Featured in Physics

Real-Time Early Detection of Crack Propagation Precursors in Delayed Fracture of Soft Elastomers

Jianzhu Ju,[1] Gabriel E. Sanoja,[1,2] Med Yassine Nagazi,[3,‡] Luca Cipelletti,[3,4] Zezhou Liu,[5] Chung Yuen Hui,[5,6] Matteo Ciccotti,[1] Tetsuharu Narita,[1,6,*] and Costantino Creton[1,6,†]

[1]*Laboratoire Sciences et Ingénierie de la Matière Molle, ESPCI Paris, PSL University, Sorbonne Université, CNRS, F-75005 Paris, France*

[2]*McKetta Department of Chemical Engineering, The University of Texas at Austin, Austin, Texas 78723, USA*

[3]*Laboratoire Charles Coulomb (L2C), University of Montpellier, CNRS, 34095 Montpellier, France*

[4]*Institut Universitaire de France, 75231 Paris, France*

[5]*Sibley School of Mechanical and Aerospace Engineering, Cornell University, Ithaca, New York 14853, USA*

[6]*Global Station for Soft Matter, Global Institution for Collaborative Research and Education, Hokkaido University, 060-0808 Sapporo, Japan*

(Received 16 September 2022; revised 21 January 2023; accepted 3 April 2023; published 26 May 2023)

The fracture of materials can take place below the critical failure condition via the slow accumulation of internal damage followed by fast crack propagation. While failure due to subcritical fracture accounts for most of the structural failures in use, it is theoretically challenging to bridge the gap between molecular damage and fracture mechanics, not to mention predicting the occurrence of sudden fracture, due to the lack of current nondestructive detection methods with suitable resolution. Here, we investigate the fracture of elastomers by using simultaneously space- and time-resolved multispeckle diffusing wave spectroscopy (MSDWS) and molecular damage mapping by mechanophore. We identify a fracture precursor that accelerates the strain-rate field over a large area (cm^2 scale), at considerably long times (up to thousands of seconds) before macroscopic fracture occurs. By combining deformation or damage mapping and finite-element simulations of the crack-tip strain field, we unambiguously attribute the macroscopic response in elastic deformation to highly localized molecular damage that occurs over a sample area of about 0.01 mm^2. By unveiling this mechanism of interaction between the microscopic molecular damage and the minute but long-ranged elastic deformation field, we are able to develop MSDWS as a flexible, well-controlled tool to characterize and predict microscopic damage well before it becomes critical. Tested using ordinary imaging and simple image processing, MSDWS predictions are proven applicable for unlabeled and even opaque samples under different fracture conditions.

DOI: 10.1103/PhysRevX.13.021030 Subject Areas: Mechanics, Optics, Soft Matter

I. INTRODUCTION

Fracture resistance of soft materials is typically characterized by a tensile test carried out until fracture, where parameters such as stretch and stress at the breaking point are commonly used. The fracture mechanics community has long used prenotched samples and defined the fracture energy, Γ in J/m^2, as the critical value of the strain energy release rate G_c, where the crack begins to propagate from the notch [1]. However, careful examination of the experimental data shows that for soft materials, where dissipation takes place over several length scales and timescales, this critical transition is not very well defined because of the presence of some slow subcritical crack propagation, and it depends strongly on the precision of the measurement. Not only can the strain energy release rate G be time dependent due to viscoelasticity of the polymer networks [2], the fracture energy Γ can also evolve with the accumulation of localized damage by fatigue [3,4], even though the latter is commonly excluded in models due to theoretical complexity and the lack of experimental methods to characterize

*Corresponding author.
tetsuharu.narita@espci.fr
†Corresponding author.
costantino.creton@espci.fr
‡Present address: Formulaction, 31200 Toulouse, France.

it [5,6]. When $G < G_c$, catastrophic fracture can still take place after a long induction time, a phenomenon known as delayed fracture [2,7,8]. Even in continuous loading conditions, where a notched sample is stretched at a constant rate, it has been commonly observed that there exists a transition from an almost undetectable crack propagation to a fast propagation mode [9–11]. Conventionally, G_c is defined as the critical energy release rate at which this transition occurs. Subcritical damage phenomena occur for $G < G_c$ [2,6] and share the same implicit hypothesis: The almost unpredictable macroscopic failure is due to the progressive accumulation of molecular damage, which may or may not be concomitant with slow subcritical crack propagation [8]. These forms of localized subcritical damage account for most of the catastrophic fracture events in real life, so the interesting and important question to address is how the transition from slow or no propagation to rapid propagation takes place, and how this transition is related to molecular damage. The goal of the present study is to investigate and understand the precursors of fracture and the early stages of crack propagation by combining the recently developed quantitative characterizations and analysis of molecular damage in elastomers [12] with a method of early detection of nanoscale motion with high temporal and spatial resolution [13].

Light scattering methods such as dynamic light scattering (DLS, for weakly scattering samples [14]) and diffusing wave spectroscopy (DWS, for turbid samples [6,15–18]) can detect motion on the nano-to-micron scale and on submillisecond timescales. Conventional DLS and DWS measurements are performed in the far-field geometry, where the detector receives light scattered from the entire illuminated sample. Furthermore, DLS and DWS use a single detector collecting the signal from a few speckles of scattered light at most. Accordingly, they lack spatial resolution and require an extensive time average, two features that make them unsuitable for systems where the dynamics are spatially heterogeneous and evolve in time, as in fracture studies. The so-called multispeckle variants of DLS and DWS (MSDLS and MSDWS, respectively) introduced in the last two decades and based on pixelated detectors relax the time average constraint and allow for time-resolved [19] or even space- and time-resolved measurements [13].

A few studies used MSDLS to detect precursors of failure in soft solids by monitoring the evolution of microscopic dynamics. The authors of Ref. [20] used time-resolved MSDLS coupled to rheology to investigate the delayed yielding of a colloidal gel under creep. A transient acceleration of the microscopic dynamics was seen and attributed, quite generically, to a "burst of microscopic plastic rearrangements." Because that experiment lacked spatial resolution and due to the relatively large length scales probed by single scattering (on the order of 1 μm), it was not possible to gain a deeper understanding of the origin of the light scattering signal. Similarly, a MSDLS investigation on a polymer hydrogel [21] revealed what was interpreted as a "wave of plastic activity" preceding failure, but once again, the origin of the light scattering signal could not be elucidated.

Several works [6,13–16] used MSDWS to study failure of (partially) amorphous systems, such as elastomers [6], semicrystalline polymers [17], and granular materials [22], where plastic rearrangements, commonly corresponding to a smooth yielding [23], occur before structural failure. As compared to other methods such as MSDLS or digital image correlation [16,18], MSDWS is particularly appealing thanks to its superior sensitivity to very small motion, down to the nm scale. Quite generally, these works revealed enhanced, spatially heterogeneous, microscopic dynamics in materials loaded beyond the mechanical linear regime. In particular, Van der Kooij *et al.* [6] have applied MSDWS to the investigation of crack growth in an elastomer. By imaging a small portion (a few mm^2) of the sample around a notch and focusing on a time window of a few seconds before rupture, they could detect enhanced dynamics on a single, fast timescale (0.5 ms), just ahead of macroscopic rupture. Unfortunately, that experiment could not address the question of the existence and origin of dynamic precursors because of the reduced space and time windows that were available and blurring effects associated with the transmission geometry that was chosen. More generally, MSDWS experiments are confronted with the challenge of interpreting the physical origin of the measured dynamics. Indeed, a variety of distinct physical mechanisms may lead to similar MSDWS signals, including spontaneous dynamics due to thermal motion, the affine or nonaffine deformation of otherwise pristine materials, or irreversible plastic events [18].

These difficulties are particularly challenging in elastomers, where plasticity and yielding are typically not easily observed. In elastomers, the absence of a well-defined yield point results in a distinctive type of damage by irreversible bond scission, which, until recently, has only been characterized macroscopically with cyclic tests showing a softening, the so-called Mullins effect [24,25]. Recently, however, molecular-level insight in failure mechanisms has been gained by inserting mechanophores in the network [12,26–28]. Mechanophores are force-sensitive molecules that emit light or become fluorescent upon bond scission. They allow the detection of damaged regions. Mechanophores have revealed that, in elastomers, bulk molecular damage occurs but only relatively close to the fracture surface [12,26], over distances of the order of tens or hundreds of microns [12,26,29–31].

Crucially, experiments with mechanophores suggest that the bulk of the elastomer remains elastic and intact. This feature naturally raises the question of the nature of the enhanced dynamics measured by MSDWS in previous experiments [6] over distances seemingly larger than those concerning bond breaking. More generally, mechanophores provide the unique opportunity to clarify the relationship between the accumulation of localized molecular damage,

the enhanced dynamics reported in previous light scattering experiments, and the (delayed) macroscopic failure.

Here, we investigate failure in a mechanically loaded elastomer of polydimethylsiloxane (PDMS), using a unique combination of the detection of localized molecular damage, simultaneous space-resolved measurements of the microscopic dynamics over the whole sample, and finite-element simulations [32,33]. We show that while bond breakage is confined to a region up to about 100 μm from the crack tip, it induces a long-ranged strain field ruled by linear elasticity that is detectable by MSDWS up to more than 1 cm from the crack tip, up to thousands of seconds before macroscopic failure. Finite-element simulations support the proposed scenario, ruling out ultraslow crack propagation as an alternative source of the MSDWS signal.

Collectively, our experiments and modeling provide unique insights on the long-range effects of molecular damage, clarifying the microscopic origin of the enhanced dynamics measured by MSDWS. Together with tests on a variety of materials under different loading conditions, they allow us to establish, on firm bases, MSDWS as an effective, versatile method for detecting and anticipating catastrophic crack growth and material failure.

II. SIMULTANEOUS MAPPING OF STRAIN RATE AND DAMAGE

Sylgard 184 polydimethylsiloxane (PDMS) is used as a model soft material, with a π-extended anthracene Diels-Alder adduct diacrylate [34] (0.1 wt%) used as a mechanophore cross-linker and TiO_2 nanoparticles (diameter 250 nm, 0.25 wt%) dispersed before curing (Appendix A). Single edge notched (SEN) samples are tested in uniaxial tension until failure with a nominal stretch rate of $\dot{\varepsilon}_N = 5 \times 10^{-5}\ s^{-1}$, in a custom-designed tensile rig, with both clamps moving symmetrically in opposite directions and fitted with the experimental setup shown in Fig. 1(a). A spatially resolved characterization of the dynamics over the whole sample surface is carried out by MSDWS in a backscattering geometry, by illuminating the sample from the bottom with an expanded laser beam. The technique detects motion in a sample slab with a thickness of several l^*, where l^* (430 μm in this case) is the photon transport mean free path. In the present case, this corresponds to about 20% of the sample thickness. Simultaneously, fluorescence from the broken mechanophore cross-linkers was detected by confocal imaging from the top, around the crack tip. Under continuous stretching, PDMS has a Young's modulus around 1.2 MPa (Fig. S1, Supplemental Material [35]), and macroscopic fracture is detected in SEN samples at a nominal strain $\varepsilon_f = 15$–16%, as detectable from bright-field imaging.

Figure 1(b) shows the 3D mapping by confocal microscopy of the fluorescence intensity due to the mechanophore activation around the original open notch, for different levels of crack opening related to applied strains. Briefly, as the sample is stretched, some of the cross-linker molecules break near the crack tip. When the mechanophore cross-linker is irreversibly broken, it becomes fluorescent under laser illumination, so the accumulated bond scission can be measured by confocal microscopy [12,36]. Previous work on poly ethyl acrylate networks [12] has shown that within this concentration range, and provided that the mechanophore is used as a cross-linker and is well soluble in the elastomer (which is the case here), the fluorescence intensity is proportional to the number of cross-linkers undergoing scission. The high quantum yield of the π-extended anthracene gives a detection limit of the

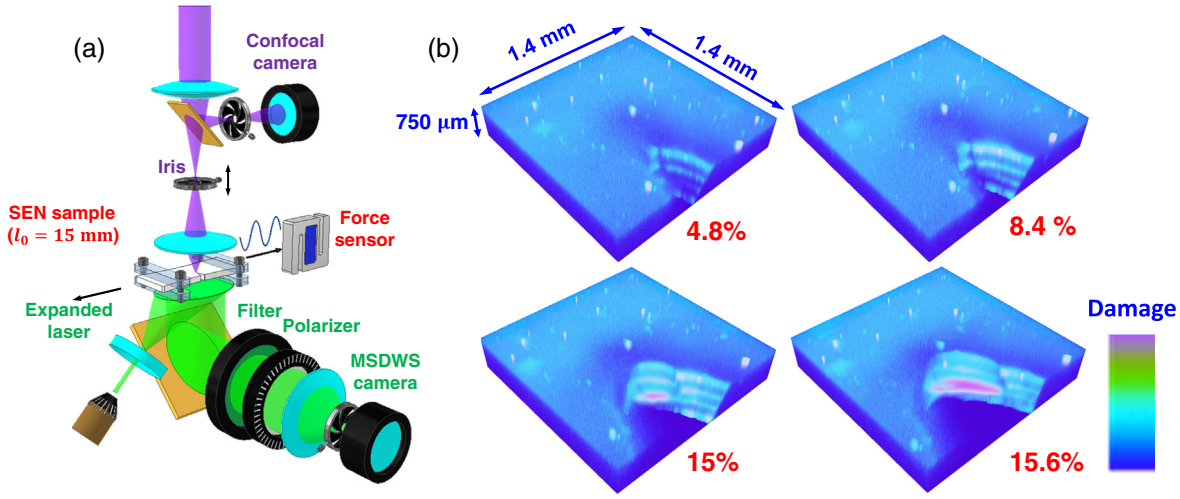

FIG. 1. (a) Setup for simultaneous MSDWS and confocal microscopy. A single edge notched sample (width 9 mm, length 15 mm, thickness 2 mm, and notch length 1 mm, cut with a fresh razor blade) is tested under uniaxial tension simultaneously mechanically, by MSDWS, and by confocal microscopy. (b) Three-dimensional image of bonds breaking around the crack tip during tensile testing of a notched PDMS sample. Four image slices (1.4 mm × 1.4 mm in plane with detection thickness 150 μm) scanning a depth of 750 μm around the midplane of the sample are collected for a single 3D image. Images are labeled by the imposed strain.

order of 1 ppm relative to the monomer unit. However, the random incorporation and activation of the mechanophore should be tested when incorporated into a completely new material.

To build each 3D image, four image slices are collected (Appendix A), and the dark strip patterns in the 3D images correspond to the gaps between slices not to the structure. In the experiment shown, fracture is observed at $\varepsilon_f = 15.6\%$. While initial activation is due to the artificial cut of the notch, images show that the activation intensity due to bond breaking increases already at strains much lower than ε_f (from 4.8% to 15%). At small $\varepsilon_N < 13\%$, the majority of the activation that is observed is due to the cutting of the notch with a sharp razor blade and does not extend beyond 50 μm away from the notch tip. From the onset of propagation [$\varepsilon_N = 15\%$ in Fig. 1(b)], massive damage is detected around the crack in the third slice, with a length of over 500 μm along the crack profile.

Area-averaged fluorescence intensities $\bar{I}$ are calculated in the third slice, within the region where $I > 2I_{\text{bulk}}$, with I_{bulk} the average fluorescence intensity in a region far away from the crack tip (see Supplemental Material for details). Then, $\bar{I}$ is renormalized by I_{bulk} to remove the influence of absorption and laser bleaching, as shown in Fig. 2(a). From the beginning of stretching, $\bar{I}/I_{\text{bulk}}$ increases slowly at an almost constant rate for $\varepsilon_N = 14\%$. At $\varepsilon_N = 14.4\%$ ($\Delta t = 240$ s before fracture), a larger increase in intensity occurs on the right side of the crack in the 2D image [inset of Fig. 2(a)], after which $\bar{I}/I_{\text{bulk}}$ increases faster. For $13.8\% < \varepsilon_N < 15.1\%$, there is a rapid increase in fluorescence intensity, but no crack propagation is detectable by bright-field microscopy imaging with submicron resolution. As seen in Fig. 2(a), a slight change in crack length Δc is detectable only starting at $\varepsilon_N = 15.1\%$ ($\Delta t = 100$ s before fracture), when the crack starts growing at an ultraslow rate of about 1.5 μm/s. A sharper crack is then nucleated 19 s before macroscopic fracture ($\varepsilon_N = 15.5\%$), at a location that matches well the region where molecular-level damage was already visualized by mechanophore mapping at smaller strains. Note that 90% of the crack propagation occurs in the last 5 s, making it extremely difficult to anticipate macroscopic fracture by conventional imaging alone.

MSDWS is used simultaneously to spatially map the microscopic dynamics by imaging the bottom face of the sample. Briefly, a characteristic relaxation rate ν_0 of the microscopic dynamics is obtained by fitting the temporally and spatially resolved intensity autocorrelation function, where larger ν_0 values correspond to faster dynamics (see Appendix A and Supplemental Material). Maps of ν_0 are built for different values of ε_N during the continuous stretching experiment and are shown in Fig. 2(b). For $\varepsilon_N < 13.7\%$, the ν_0 maps remain almost identical, with slightly higher values of ν_0 around the crack tip, where the faster dynamics region progressively develops to the right, consistent with the molecularly damaged

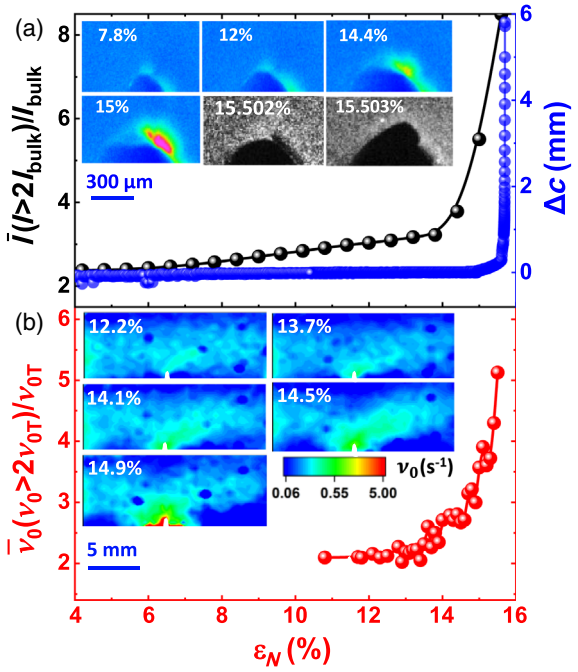

FIG. 2. (a) Main plot: black, averaged intensity $\bar{I}$ of mechanophore activation, in the region with $I > 2I_{\text{bulk}}$ (defining activated fluorescence after deformation), renormalized by the bulk intensity I_{bulk}. Blue: crack propagation length Δs. Insets: 2D mechanophore maps at 400 μm deep from the sample surface. For images at the onset of macroscopic propagation (15.502% and 15.503%), a confocal microscope cannot capture the images due to its low time resolution, so raw images from the MSDWS camera are shown instead. (b) Main plot: averaged value of the normalized relaxation rate $\bar{\nu}_0/\nu_{0T}$ (red) measured by MSDWS in the region $\nu_0 > 2\nu_{0T}$. Inset: ν_0 maps at different ε_N. Note that the field of view in MSDWS is about 20 times wider than in confocal microscopy.

region detected by fluorescence confocal microscopy in Fig. 2(a). For $\varepsilon_N > 13.7\%$ ($\Delta t = 380$ s before fracture), a significant acceleration of the dynamics occurs in front of the crack and grows rapidly.

Crucially, by coupling the MSDWS measurements to the mechanophore signal, we can quantitatively interpret the light scattering data. The confocal images show that cross-linker scission is localized within about 200 μm from the crack tip. The enhanced dynamics detected by MSDWS occurs over a much larger region (about 1 cm from the tip), where the network is intact. Thus, the MSDWS signal must correspond to the elastic response of the pristine elastomer network to localized breakage, rather than to structural changes directly resulting from widespread bond scission. With this in mind, we can now relate the MSDWS measurements to the long-range strain-rate field induced by the bond-breaking events localized near the crack tip. It can be shown (see Supplemental Material) that measured dynamics under these conditions can be well described by $\nu_0 = \sqrt{3}kl^*\sqrt{\text{Tr}(\boldsymbol{D}^2)}$, where k is the laser-light wave vector and $\boldsymbol{D}$ is the symmetric part of the velocity gradient

tensor in the deformed state (namely, the rate of deformation tensor [18,37–39]). The absolute strain-rate value corresponding to the measured ν_0 can be calibrated by determining the setup and sample-dependent constant kl^* in uniformly deformed, un-notched samples [18], where ν_0 is proportional to the true strain rate along the stretch direction, $\dot{\varepsilon}_T$ (see Supplemental Material). An applied $\dot{\varepsilon}_N = 5 \times 10^{-5}$ s^{-1} corresponds to $\nu_{0N} = 0.23$ s^{-1}, and $\dot{\varepsilon}_T$ corresponds to $\nu_{0T} = \nu_{0N}/(1+\varepsilon_N)$. Since ν_0 is proportional to the (local) strain rate, here and in the following, we use it as a proxy for the deformation rate. The averaged value $\bar{\nu}_0$ in the region with $\nu_0 > 2\nu_{0T}$ [roughly, the green region in the maps in the inset of Fig. 2(b)] is calculated and shown in Fig. 2(b), after normalization by ν_{0T}. Note that $\bar{\nu}_0/\nu_{0T}$ starts increasing at $\varepsilon_N = 13.5\%$ ($\Delta t = 420$ s before fracture) and reaches a large value of 4 at $\varepsilon_N = 15\%$, where the area with $\nu_0 > 2\nu_{0T}$ extends over 10 mm^2.

As a further demonstration that in our experiments the MSDWS dynamics is modified by the long-range strain-rate field set by localized damage, we compare the MSDWS results to a more conventional quantification of the strain field obtained, on a separate sample, by a classical digital imaging correlation method (DIC). The MSDWS and DIC tests follow the same protocol: Different samples with identical geometries (size 2 cm × 4 cm × 4 mm, crack length $c = 2$ mm) are subjected to uniaxial extension at $\dot{\varepsilon}_N = 1.25 \times 10^{-4}$ s^{-1} until failure. DIC measures spatially resolved deformation fields by comparing images of the sample surface during the elongation test. In order to resolve all components of the 2D strain-rate tensor $\boldsymbol{D}$, the sample is sprayed with black ink, which forms a speckled pattern, whose displacement is then tracked. Next, $\boldsymbol{D}$ is calculated with images collected from time t to $t+T$ (by a program customized from open source project pydic [40]; see Supplemental Material for details), where T is the time interval for correlation and averaging.

Because of the lower detection sensitivity of strain heterogeneity of DIC, the minimum required time $T_{\min}$ between images to obtain a reliable signal is much longer compared to the $\tau_0 = 1/\nu_0$ (~0.2 s) around the crack tip, the characteristic decorrelation time of the autocorrelation function. In Fig. 3(b), we applied the values $T = T_{\min}$, which are 20 s, 10 s, and 4 s, respectively.

For the sake of comparison with MSDWS, the strain-rate tensor obtained by DIC is used to calculate the relaxation rate $\nu_0(\boldsymbol{D})$, i.e., the same quantity that is directly measured by MSDWS. The ν_0 maps obtained by MSDWS and DIC are shown in Figs. 3(a) and 3(b), respectively, for the same times before full fracture (the sample tested with MSDWS failed at $\varepsilon_f = 15.9\%$ while the sample tested with DIC failed at $\varepsilon_f = 15.7\%$). The quantitative similarity between both maps is evident, thus confirming that the dynamics measured by MDWS are due to modifications of the long-range strain field induced by localized bond breaking and validating the use of MSDWS to quantitatively map strain rate, including in a complex 2D geometry with a notch.

To summarize, both mechanophore mapping of molecular damage and MSDWS dynamics mapping show that during a long induction period, from around $\varepsilon_N \sim 13.5\%$ to just before the rapid crack propagation, there are detectable microscopic precursor events, whose characteristic size progressively grows, while no macroscopic failure occurs. Remarkably, while bond breaking occurs only very close to the crack tip, over a sample area of around 0.01 mm^2, the resulting strain field can be simultaneously detected by MSDWS and DIC over a much larger area, of the order of a sample size of around 20 mm^2. At the stretch rate applied here, the precursors highlighted by both methods are observable about 7 min before macroscopic fracture, clearly demonstrating their predictive power.

III. FINITE-ELEMENT MODELING RULES OUT ANY CONTRIBUTION OF SLOW CRACK PROPAGATION TO THE STRAIN FIELD

Naturally, localized damage plays an important role in crack propagation, but in existing continuum models, it is

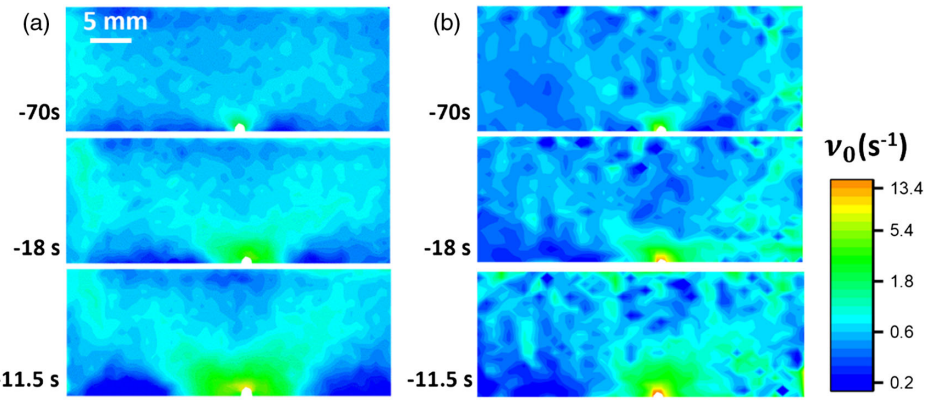

FIG. 3. Maps of the relaxation rate ν_0 calculated from MSDWS (a) and DIC (b) at different times before fracture for two distinct samples stretched at $\dot{\varepsilon}_N = 1.25 \times 10^{-4}$ s^{-1}.

theoretically challenging to couple damage and deformation [41]. An important question raised by our experiments is whether the increase in strain rate measured by MSDWS far from the crack tip is (i) due to the combined effect of sample loading and a slow crack growth that may go undetected because of image resolution limitations or (ii) the result of the localized molecular damage detectable by fluorescence. To address this question, for the same model PDMS, we carry out a full-field finite-element method (FEM) simulation. It must be noted that the FEM simulation considers only the contribution of deformation and crack propagation and does not account for changes in local material properties due to molecular-level damage. We use a neo-Hookean solid material model [42] with parameters fitted to the uniaxial tension data to calculate the full-field strain rate. To examine whether the measured increase in strain rate is due to undetectable slow crack growth, we perform a FEM simulation with a stationary crack and with a slowly growing crack at different speeds, respectively. Propagation is simulated by introducing an increasing crack length from the stationary crack position, otherwise leaving all material properties unchanged. The FEM results are compared to the DIC measurements described in the previous section, by plotting the strain rate along the stretching direction, $D_{\mathrm{xx,\,FEM}}$ and $D_{\mathrm{xx,DIC}}$ for FEM and DIC, respectively, as a function of y, for fixed $x = 0$ [see inset in Fig. 4(a)].

Results without and with crack propagation are shown in Figs. 4(a) and 4(b), respectively: In both cases, $\dot{\varepsilon}_N = 1.25 \times 10^{-4}\ \mathrm{s}^{-1}$. In the absence of propagation, $D_{\mathrm{xx,FEM}}$ far from the tip ($y > 0.1$ mm) remains almost the same up to $\varepsilon_N \sim 20\%$ (the sample does not break in simulations). However, while at low strain the experimental $D_{\mathrm{xx,DIC}}$ and numerical $D_{xx,\mathrm{FEM}}$ match well, starting from $\varepsilon_N = 15\%$, $D_{xx,\mathrm{DIC}}$ is significantly larger than $D_{xx,\mathrm{FEM}}$, even millimeters ahead of the tip, without any experimentally detectable propagation of the crack, indicating the existence of a fracture precursor, as discussed in relation to Fig. 2. In Fig. 4(b), we use our FEM result to test whether the strain-rate field measured in experiments could be due to crack propagation alone. Even if one assumes a crack speed $\dot{c} = 0.01$ mm/s in the simulation (1 order of magnitude above the optically detectable crack speed $\dot{c} \sim 0.001$ mm/s) Note that $D_{\mathrm{xx,DIC}}$ is still well above $D_{xx,\mathrm{FEM}}$ at $\varepsilon_N = 15\%$ [Fig. 4(b)]. Furthermore, at a slightly larger strain of $\varepsilon_N = 15.3\%$ (24 s later), still without any experimentally detectable crack propagation, a dramatic increase of $D_{\mathrm{xx,DIC}}$ is observed, once again not captured by FEM.

In summary, at small values of applied ε_N, the comparison between simulation (FEM) and experiments (MSDWS/DIC) shows excellent consistency. However, for higher values of ε_N approaching macroscopic fracture, the experimental values deviate largely from FEM simulations. These results, combined with the MSDWS and

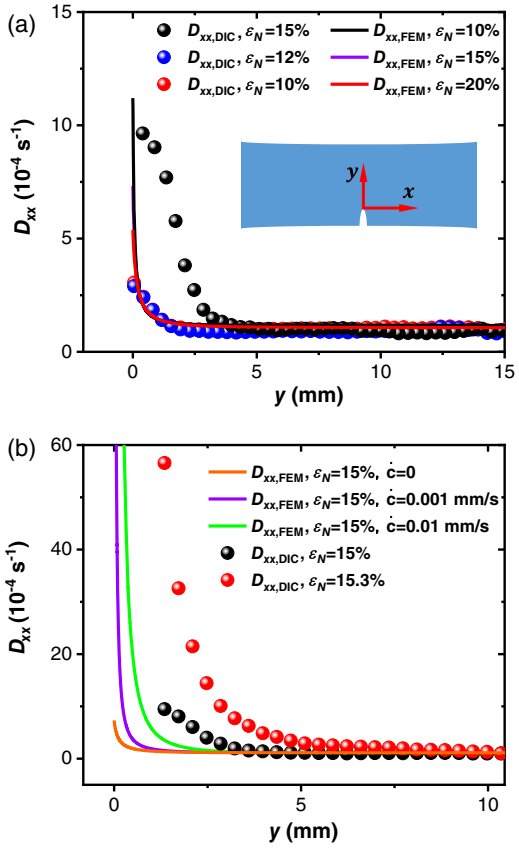

FIG. 4. (a) $\boldsymbol{D}_{xx}$ component of the rate of deformation tensor as a function of distance y from the crack tip, for $x = 0$ [see the definition of axes x and y in the inset of (a)], as obtained by DIC (symbols, experiments) and FEM (lines, simulations). In panel (a), FEM data were obtained assuming that the crack tip does not move. (b) Same as in panel (a) but focusing on the late stages of the tests and implementing crack-tip propagation in FEM, at various propagation speeds $\dot{c}$, as indicated by the labels.

mechanophore mapping, demonstrate that the acceleration of the local strain rate over a large sample volume corresponds to the elastic response of the material to chemical bond scission localized very close to the crack tip. While ε_N, itself, significantly influences D_{xx} only in a region very close to the crack tip (Fig. 11, Appendix B), the rapid growth in strain rate before fracture shows a strong instability in response to dynamic damage accumulation. Note that the damage accumulation can be observed at lower ε_N [Fig. 2(a)] but only leads to an acceleration of the strain rate and fracture after $\varepsilon_N > 13.5\%$, suggesting a threshold level of damage above which propagation can be initiated. This threshold of damage level appears distinct from that predicted by the Lake-Thomas model [43], which considers bond scission only over one network mesh size (10 nm) ahead of the crack as the threshold [44]: In our experiments, by contrast, the damage zone size extends over a distance of about 200 μm [Fig. 2(a)] from the fracture surface. This may be due to the well-known presence of silica nanoparticles in the Sylgard 184 that

delocalize the damage [34]. More generally, our findings highlight the crucial need to include the effect of bond scission, which is absent from most FEM models and typically not considered in similar theoretical [2,5] and experimental works [6,7] addressing subcritical fracture.

IV. DAMAGE PREDICTION WITH MSDWS DYNAMIC ACTIVITY MAPS

A. Damage prediction in continuous condition

The observation of the large-scale strain-rate acceleration in response to damage close to the crack tip suggests that damage may be predicted, and thus prevented, by inspecting only the elastic response by MSDWS at a very early stage and far from the crack tip, before the appearance of any macroscopic structural failure. Note that, in principle, full-field DIC can provide similar information in terms of strain (rate) distribution, but the raw output of DIC is the displacement field of the grid elements into which the sample image is divided. The resolution depends on the spray-painted speckle quality, resulting in a strain precision of around 10^{-3} [45–48]. By contrast, MSDWS directly detects the intensity time decorrelation due to the change in strain tensor in the deformed configuration [17], providing a strain precision up to 10^{-6} [18]. In addition, compared to painted speckles, laser speckles are independent of the deformation scale, so even the large strain regime can be well captured [17]. For hydrogels or emulsion systems with a high volume fraction of liquid, MSDWS provides an alternative method to measure the magnitude of the displacement without the need for spray painting [49]. Finally, MSDWS typically requires a shorter time than DIC to obtain a signal. Therefore, we introduce an alternative to strain-rate mapping, by calculating only the correlation values calculated at one single time lag, τ_{MSDWS}, to build dynamic activity maps (DAMs) [13,18]. The time needed to build a DAM in our experiments (typically $\tau_{\mathrm{MSDWS}} \sim 0.05/\nu_0$ is required) is about 100 times faster than what is required to obtain the same information by DIC since only a simple calculation between two images is required to visualize the transient strain-rate distribution.

We realize a prototype test on a mechanophore-labeled PDMS sample with five nominally identical notches, as shown in Figs. 5(b)–5(d), stretched at $\dot{\varepsilon}_N = 5 \times 10^{-5}\ \mathrm{s}^{-1}$ according to the protocol illustrated in Fig. 5(a). Each notch is cut with a fresh blade (scalpel blades #11) to exclude, as much as possible, the additional influence from variation in crack geometry. We process the speckle images in real time, obtaining DAMs simultaneously with the mechanical test, using $\tau_{\mathrm{MSDWS}} = 0.75$ s. Including the time for DAM computing and image saving (for later reference), an optimized time resolution of 1 s is achieved. The DAMs are visually inspected on the fly to monitor local damage, and stretching is stopped when a precursor is identified.

Like the results in Fig. 2(b), a dynamic precursor is seen during the first loading ramp, here at a strain $\varepsilon_p = 22.3\%$ (for multiply notched samples, the strain at failure ε_f is found to be larger than that for samples with one single notch). Remarkably, significant differences between the five notches can be detected: At $\varepsilon_p = 22.3\%$, only notch V is accompanied by a fast dynamic region, reaching a size of about 2 mm^2 [Fig. 5(b)]. As soon as the DAMs reveal a dynamic precursor, the stretching ramp is stopped, and the sample is unloaded and removed from the tensile stage for inspection of the five notches under confocal microscopy. The results for notches III and V are shown in Fig. 5(c), which compares the mechanophore signal for the pristine sample, before any loading, to that after the first stretching ramp. Obvious activation can only be detected in front of notch V, the same one that displayed a fast dynamics region in the DAM. Upon reloading [second strain ramp in Fig. 5(a)], the final fracture occurs at notch V [Fig. 5(d)], as suggested by the localization of the fast dynamics previously measured with real-time DAMs.

When repeating a similar experiment, but stopping the second stretching ramp at the precursor strain ε_p and then holding the sample at fixed strain, the crack never propagates within an observation time of 1 h. By contrast, when applying the same protocol of Fig. 5(a) (i.e., loading the sample until fracture during the second stretching ramp), we find a strain at fracture ε_f around 2% larger than the precursor strain ε_p. We conclude that the occurrence and location of macroscopic failure are successfully predicted, with a warning in macroscopic strain of 2% (400 s in time with our strain rate), at the stage where only a very small amount of molecular damage can be observed by confocal microscopy [Fig. 5(c)]. Several repetitions of the experiments are shown in Figs. S12 and S13 in the Supplemental Material.

B. Damage prediction in static conditions

Here, we report the predictive capacity of MSDWS for notched samples under continuous loading: a test protocol designed to predetermine, to some extent, both the location and time (or strain) of macroscopic failure. In real-life applications, one is more interested in the following: (i) long-time-delayed (hours or even days) fracture under low external loading and (ii) the detection of an internal flaw at an *a priori* unknown location, rather than at an artificial notch.

To test the predictive power of MSDWS under those conditions, the evolution of the molecular damage and of dynamics localization are simultaneously observed in a situation where SEN and un-notched samples are stretched to different strains in a step-by-step fashion and held there for measurement, with a long waiting period during in-between steps.

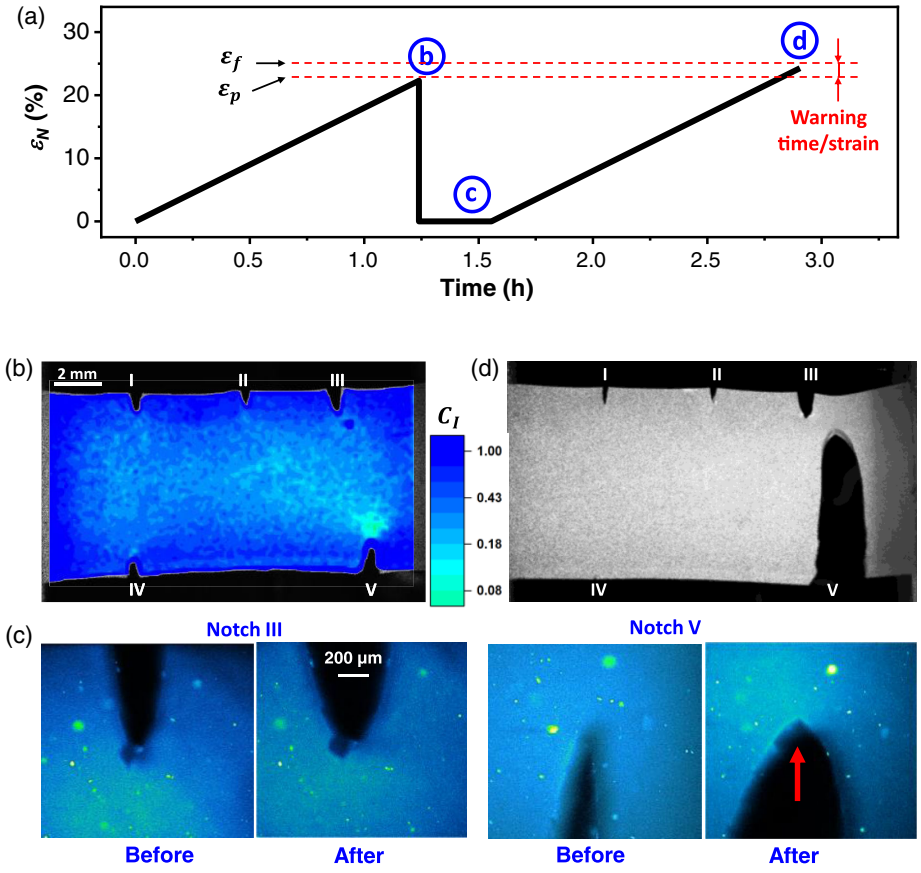

FIG. 5. (a) Prototype test of the predictive capability of MSDWS. Letters corresponding to maps taken at different stages of the experiment are indicated in the strain-time curve. For both stretching ramps, the strain rate is $\dot{\varepsilon}_N = 5 \times 10^{-5}$ s^{-1}. (b) Real-time DAM obtained at $\varepsilon_N = 22.3\% = \varepsilon_p$, using $\tau_{\mathrm{MSDWS}} = 0.75$ s. The DAM reveals the formation of a dynamic precursor localized ahead of notch V. (c) Mechanophore mapping after unloading: notches III (for which the DAMs showed no enhanced dynamics) and V (for which the DAMs showed enhanced dynamics) after the first stretching ramp ($\varepsilon_N = \varepsilon_p$), compared to the pristine sample ($\varepsilon_N = 0$) as a reference. The sample was slightly opened (much less than ε_p) for a better visualization of activation. (d) Final fracture during the second loading ramp, at a strain $\varepsilon_f \sim \varepsilon_p + 2\%$. [See horizontal dashed lines in panel (a).]

In the notched sample, the macroscopic strain is carefully increased by steps of $\Delta\varepsilon_N = 2.5\%$ maintained for 1 h, and above $\varepsilon_N = 12.5\%$, smaller steps ($\Delta\varepsilon_N = 0.625\%$) still maintained for 1 h, are chosen to ensure delayed fracture at a fixed displacement [6,7] instead of fracture during the loading step in uniaxial tension.

At $\varepsilon_N = 15\%$ (Fig. 6), a slight propagation is initially detected around $t_w = 1800$ s (the waiting time t_w is defined as the time elapsed since the end of each displacement step), with ultraslow propagation without fracture after 5 h. The initial growth of the crack is only detectable by mechanophore imaging with submicron resolution. On the other hand, DAMs show a fast dynamics region, revealing the acceleration of the strain rate around the crack tip, which starts to develop at; see Fig. 6(a). Note that for delayed fracture at fixed strain, an experiment where bulk dynamics is dominated by relaxation rather than by strain rate would require a method employing a renormalized τ_{MSDWS} to better visualize crack localization, as discussed in Appendix C. At really long t_w as in Fig. 6, bulk dynamics is much slower than crack dynamics, so a constant $\tau_{\mathrm{MSDWS}} = 40$ s can be applied here for simplicity. The area with dynamics much faster than the bulk region [defined as $C_I - \mathrm{B} < 100(C_I(\tau_0) - B)$] is calculated and shown in Fig. 6(b), together with the renormalized damage I/I_{bulk} (of the 50 μm × 50 μm area in the eventually damaged region) by mechanophore imaging and the crack length increase Δc. The onset of ultraslow crack propagation ($dc/dt \sim 20$ nm/s) starts at $t_w = 1700$ s, accompanied by a small increase of I/I_{bulk} revealing a slight increase of fluorescence intensity due to mechanophore activation. The extent and magnitude of the faster dynamic activity in DAMs further develops with t_w, reaching 3 mm^2 at 3000 s, while the steady propagation remains slow and only reaches 100 μm after 5 h (Fig. 16). Remarkably, well before the slight crack propagation ($\Delta c < 10$ μm) and damage accumulation (~20 μm), the localization signal in DAM is already macroscopically visible, starting from $t_w = 800$ s.

A similar behavior is observed in an additional test on an un-notched PDMS sample with a rectangular shape, to

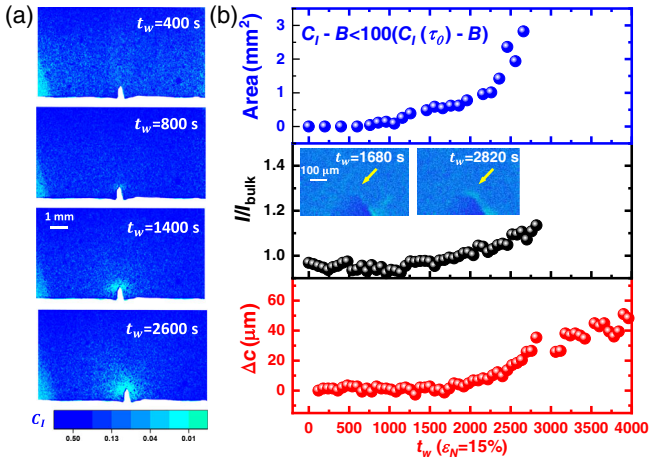

FIG. 6. (a) DAMs obtained by plotting C_I values from MSDWS at different waiting times t_w, with a fixed $\tau_{\mathrm{MSDWS}} = 40$ s. (b) Time evolution of precursors of failure inferred from MSDWS (top), mechanophore signal (middle), and crack imaging (bottom), respectively. Top: area in the DAM where the dynamics are much faster than in the bulk (see text for definition). Middle: renormalized fluorescence intensity due to mechanophore activation I/I_{bulk}. Bottom: propagation length of the crack as a function of t_w. Inset of the middle panel: 2D confocal images showing the mechanophore signal at 1680 s and 2820 s, respectively.

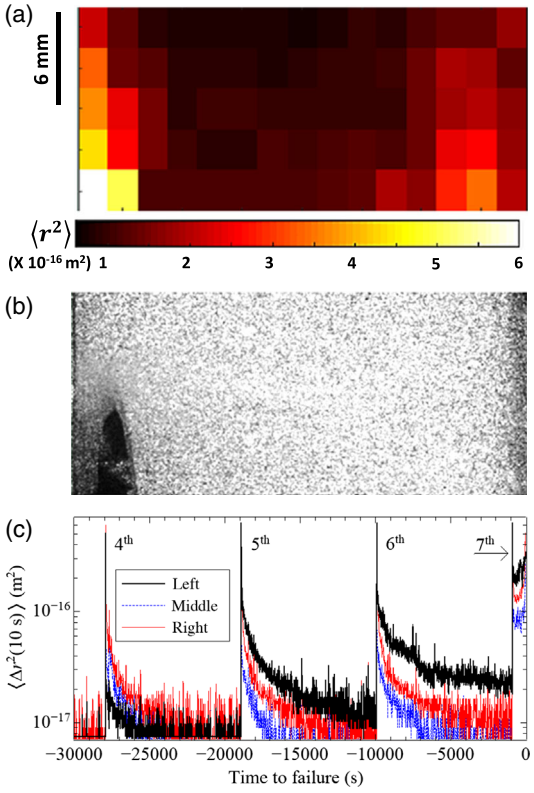

FIG. 7. (a) DAM obtained for an un-notched PDMS sample submitted to a series of strain steps, 20 s after imposing the seventh step ($\varepsilon_N = 23.1\%$). The DAM is obtained using $\tau_{\mathrm{MSDWS}} = 10$ s. (b) Speckle image taken during fast crack propagation, which occurred 910 s after the DAM shown in panel (a). Note that the crack starts from the bottom-left corner of the sample, where the DAM revealed faster dynamics almost 1000 s before. (c) Mean-squared displacement $\langle \Delta r^2 \rangle$ over a time delay $\tau_{\mathrm{MSDWS}} = 10$ s, averaged over the leftmost, the central, and the rightmost column of the DAM shown in panel (a), as a function of time before failure. For the sake of clarity, only relaxation phases 4 to 7 are shown. Failure occurs at $t = 0$ in the figure, about 900 s after the seventh relaxation phase.

avoid *a priori* strain localization. Here, we use a distinct MSDWS setup (Fig. S14 in the Supplemental Material), based on a design similar to that of Fig. 1(a). We impose seven strain steps of nominal strain amplitude 3.3% each, at a strain rate of 3.3×10^{-2} s^{-1}. After each step, the sample is held at a fixed strain for 9000 s, and the microscopic dynamics are quantified by DAMs of the microscopic mean squared displacement $\langle \Delta r^2 \rangle$ [15] obtained from the C_I signal, using $\tau_{\mathrm{MSDWS}} = 10$ s (see more details in the Supplemental Material).

The DAM taken 20 s after the beginning of the seventh rest phase (nominal strain $\varepsilon_N = 23.1\%$), shown in Fig. 7(a), reveals enhanced dynamics (larger $\langle \Delta r^2 \rangle$) as compared to those in the initial phases of the experiment, as well as strong spatial heterogeneity. The dynamics are significantly faster close to the grips, suggesting that the sample has been weakened in these regions when it was mounted in the setup, although no signature of potential weakening could be detected macroscopically. Indeed, the act of clamping the sample during tensile tests induces a stress concentration, and this is a long-standing question in experimental mechanics [50,51]. However, while one may expect damage and stress concentration to occur in all four corners of the stretched sample, we find that the dynamics are faster in the bottom part of the left grip ($\langle \Delta r^2 \rangle \sim 6 \times 10^{-16}$ m^2), precisely where macroscopic failure will eventually occur, almost 1000 s later [Fig. 7(b)].

In order to further demonstrate the predictive power of MSDWS applied to fracture problems, we plot in Fig. 7(c) the time dependence of $\langle \Delta r^2(10\ \mathrm{s}) \rangle$ averaged over three sample strips, near the two clamps and in the middle. Data for the fourth relaxation phase are representative of the behavior at small strains: After each pulling step (identified by the large overshoot of the mean squared displacement), $\langle \Delta r^2 \rangle$ decays over a few thousands of seconds, with no notable differences according to the sample area. By contrast, starting from the fifth relaxation phase, the decay of $\langle \Delta r^2 \rangle$ slows down while dynamic activity is enhanced close to the grips. The sixth relaxation phase confirms this trend, until the seventh relaxation phase, where the dynamics near the grips are sped up by almost a factor of 10 and accelerate until sample failure, rather than slowing down as in the previous phases. Starting from the sixth relaxation phase, the dynamics close to the left grip are consistently faster than those close to the right grip, providing a warning

on where the sample will eventually fail several thousands of seconds later.

Note that, in this test, the sample is at rest during the relaxation phases, which would make it difficult to obtain a measurable DIC signal since $T_{\min}$, the required time interval for correlation, would likely become longer than the duration of each step.

Thus, these tests in static conditions demonstrate the great sensitivity of MSDWS as a tool to anticipate macroscopic fracture in static subcritical loading. Finally, we note that for these studies, since the bulk dynamics of the material is dominated by relaxation, the correspondence between DAMs and mechanical parameters is rather complex. In these cases, DAM is only employed as a qualitative visualization to characterize the level of localization.

C. Extension of the method to different materials

The detection of a large-scale dynamic precursor was illustrated in the previous sections for a PDMS elastomer, but similar precursors exist in different materials. To demonstrate the generality of the results reported for PDMS,in Appendix C 1, we show data for a poly (ethyl acrylate) network, an elastomer with a very standard network structure but an entirely different chemistry as compared to PDMS. As for PDMS, we find that MSDWS allows for detecting the large-scale elastic response to localized microscopic molecular damage.

MSDWS can detect microscopic damage with excellent temporal resolution, with the only requirement being a highly scattering material with no strong absorption of light. This is a common feature of many soft materials due, e.g., to the presence of fillers or structural features of a length scale of the order of the wavelength of visible light. The method can be used for semicrystalline polymers [17], filled soft materials [52], or any transparent material to which a small amount of high refractive index probe particles can be added before shaping. We show here two examples of testing the onset of fracture in raw materials, where no added probe particles are necessary. The first example concerns a SEN sample of natural rubber, where impurities provide multiple scattering, which was submitted to uniaxial extension at a rate $\dot{\varepsilon}_N = 2 \times 10^{-4}$ s^{-1} (Fig. 8). A sideway propagation [53] of the crack, classically observed in natural rubber due to strain-induced crystallization [54], is observed at $\varepsilon_N = 25\%$, where the crack starts propagating to the left of the notch (red arrow). Remarkably, a fast dynamics region with a length of about 2 mm can already be detected precisely in that region by inspecting a DAM measured at $\varepsilon_N = 17\%$, 400 s before any propagation can be detected by direct imaging.

The second example concerns crack propagation in a piece of notched dry tagliatelle pasta, stretched at $\dot{\varepsilon}_N = 10^{-4}$ s^{-1}, where ductile fracture starts from a very small strain, as shown in Fig. 9. Interestingly, the somehow

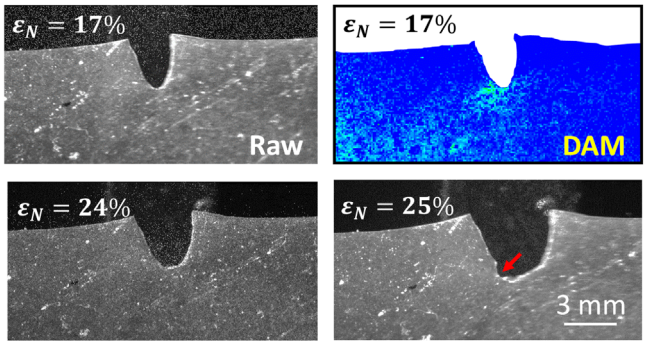

FIG. 8. Prediction of "sideway" propagation in natural rubber.

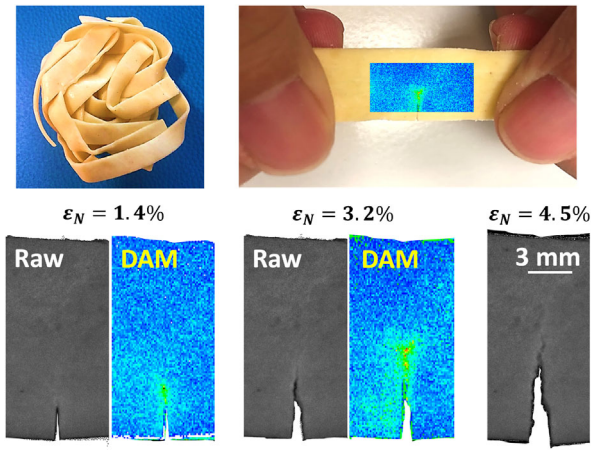

FIG. 9. Raw images and DAMs during the propagation of a piece of notched tagliatelle pasta (with egg).

tortuous propagation path can be well predicted by DAMs collected at lower applied strain.

Note that in these materials, localized dynamics are not necessarily due to changes in strain rate only since MSDWS detects multiple contributions to the dynamics [17]. Details of the experiments in Figs. 8 and 9 are provided in the Supplemental Material.

V. CONCLUSIONS

During the fracture of PDMS elastomers, MSDWS reveals an acceleration in local dynamics up to thousands of seconds before macroscopic fracture. Unlike in previous MSDWS works where early detection of failure was not possible [6,17,20], or MSDLS measurements where the microscopic origin of the enhanced dynamics remained unclear [6,17,20,21], here we unambiguously show that the MSDWS signal stems from the global elastic response of the material to local damage. FEM simulations and mechanophore mapping confirm this scenario: The elastic response over cm^2 is caused by the localized accumulation of molecular damage over a threshold (~0.01 mm^2 in area around the crack tip), after which it gradually grows and leads to macroscopic fracture. Thus, the precursor we

reported here takes place in an elastic and reversible form: If the load is released upon the detection of the precursor, the same region in the material will behave as if there was never molecular damage.

The ability of MSDWS to detect and quantify displacements on short timescales and very small length scales—yet imaging a large field of view—is crucial for the early detection of the elastic response to localized damage. It distinguishes MSDWS from single scattering techniques and digital imaging correlation methods. These features make MSDWS a promising and convenient nondestructive tool for early-stage detection and prevention, especially for elastomers, where microscopic damage can be characterized by examining the elastic response in the *undamaged* region. Potentially, the performance of the detection of the localization by simple processing of ordinary low-resolution imaging could be largely enhanced with machine-learning methods [55], and with a defined threshold for acceptable warning time, macroscopic fracture may be predictable even without knowing the details of the material.

Data Availability: ASCII and images provided in all the figures in the main text and Supplemental Material have been uploaded in Zenodo [56].

ACKNOWLEDGMENTS

This work was funded by the European Union's Horizon 2020 Program for Research and Innovation under the Marie Skłodowska-Curie Grant Agreement No. 765811 (DoDyNet) and Grant Agreement AdG No. 695351 (CHEMECH). This work was partially supported by ANRT (Grant No. 2014/0109) and ANR MultiNet (Grant No. ANR-20-CE06-0028-01). L. C. gratefully acknowledges support from the Institut Universitaire de France. The authors thank Liangbin Li for kindly providing the natural rubber sample.

APPENDIX A: MATERIALS AND METHODS

1. Material preparation

PDMS elastomers were prepared from PDMS Sylgard 184 (Dow Corning) with a 10:1 ratio of PDMS base and curing agent. First, 4 g of PDMS base was mixed with titanium dioxide (TiO_2) nanoparticles (diameter 250 nm, 10 mg) and sonicated for 10 minutes to avoid aggregation of the nanoparticles. Curing agent (0.4 g) and Diels-Alder adduct mechanophore (5 mg, dissolved in 1 g toluene) were then added and mixed well by vortexing for 10 minutes. The mixture was then poured in a mold to prepare a film and cured in vacuum at 90 °C for 8 h so that toluene can be evaporated during curing. The material composition is shown in Fig. 10(a). The synthesis of the Diels-Alder adduct mechanophore [Fig. 10(b)] was originally reported by Göstl *et al.* [36] and described in detail in Ref. [12]. As the mechanophore cross-linker is under tension and irreversibly broken, it becomes fluorescent under laser illumination with a wavelength of 405 nm, so the accumulated bond scission can be quantified by measuring the fluorescence intensity [12,36].

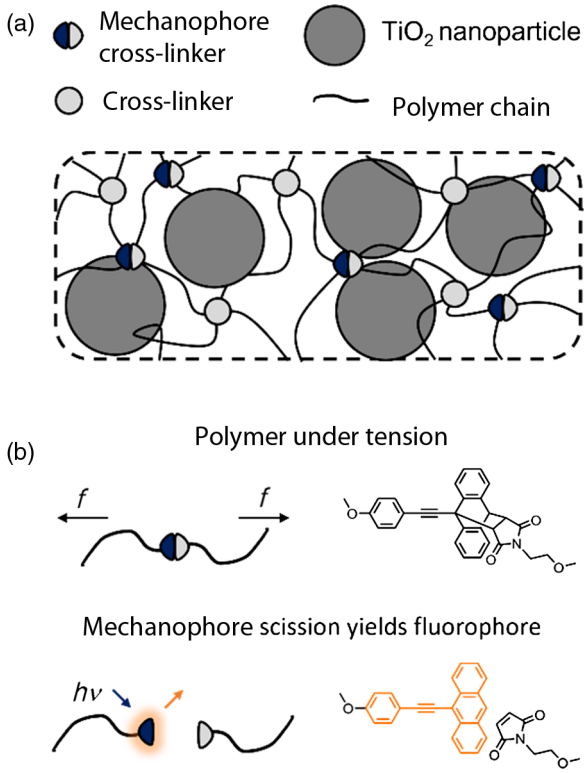

FIG. 10. (a) Material composition of PDMS with the addition of mechanophore cross-linker and nanoparticles. (The schematic is not to scale since the TiO_2 nanoparticle should be significantly larger than the mesh size.) (b) Fluorescence mechanism of mechanophore cross-linker in polymer under tension.

2. Confocal microscopy

Confocal microscopy (Nikon AZ-100/C2+ confocal macroscope) was applied to map 3D fluorescence intensity due to damage. We used an AZ Plan Fluor 5 × objective, with a focal length of 15 mm. The objective was zoomed in 3×, with a field of view of 1.4 × 1.4 mm and image resolution of 0.68 μm/pixel (image size 2048 × 2048 pixel^2) in the plane. Excitation and emission collection wavelengths were 405 nm and 450–520 nm, respectively. In scanning confocal microscopy, a relatively long exposure time is required to acquire depth-resolved images with enough resolution and intensity, so time resolution is poor. Furthermore, the fluorescence intensity of the activated mechanophore can be bleached after a long exposure under laser illumination. Considering the trade-off between image quality and time resolution and the need to avoid photobleaching, only four slices (thickness 150 μm with exposure time 8 s) are scanned for each 3D image, with a depth resolution of 200 μm and time resolution 2 min/scan, where images are collected at the beginning of each scan. The total

scan thickness is 750 μm, situated around the midplane in the thickness direction of the sample. Quantification of the data is described in the supplemental material.

3. Multispeckle diffusing wae spectroscopy

Time-resolved imaging of the whole sample was simultaneously performed with MSDWS, with a better time resolution (100 ms) but a worse spatial resolution [size of the region of interest (ROI): 0.3 mm × 0.3 mm, magnification = 0.01 mm/pixel] compared to confocal microscopy. The technique detects motion in a sample slab of several l^* thickness, the photon transport mean free path [57]. In the present case, l^* is around 430 μm in the PDMS sample (20% of the sample thickness), measured in a suspension containing TiO_2 nanoparticles with the same volume concentration as in the elastomers [18]. For all MSDWS data except those of Fig. 7, the setup of Fig. 1(a) was used: The whole surface of the sample was illuminated homogeneously by an expanded green laser (wavelength 532 nm), and the speckle images were collected by a CMOS camera (BASLER acA2000–340 km). The spatially resolved in-plane strain rate at the surface of the polymer network can be quantified from the autocorrelation function of the multiply scattered light intensity:

$$C_I(\vec{r},t,\tau)=\frac{\langle I_p(t)I_p(t+\tau)\rangle_{\vec{r}}}{\langle I_p(t)_{\vec{r}}I_p(t+\tau)\rangle_{\vec{r}}}-1, \tag{A1}$$

where t and τ are the experimental time and the time interval for correlation, respectively. Note that $I_p(t)$ is the intensity at the pth pixel, and $\langle\ldots\rangle_{\vec{r}}$ provides the average over a ROI with a center position at $\vec{r}$. The characteristic decorrelation time τ_0 of the autocorrelation function corresponds to the time over which the probe is displaced by $1/k$ (k is the wave vector), around 50 nm. At fixed t and $\vec{r}$, τ_0 can be obtained by fitting C_I to [58]

$$C_I(\tau)=A\exp\left(-2\gamma\sqrt{\left(\frac{\tau}{\tau_0}\right)^p+a}\right)+B, \tag{A2}$$

and the characteristic decorrelation rate is defined as

$$\nu_0=1/\tau_0. \tag{A3}$$

This decorrelation rate can then be related to the deformation rate by

$$\nu_0=\sqrt{3}kl^*\sqrt{f[\boldsymbol{D}]}, \tag{A4}$$

which is applied to visualize the two-dimensional (2D) strain-rate distribution. Here, $\boldsymbol{D}$ is the rate of deformation tensor [37], and $f[\boldsymbol{D}]=2\mathrm{Tr}(\boldsymbol{D}^2)/15$ [6,17]. Under uniform deformation in uniaxial tension, ν_0 can be directly related to the true strain rate, as reported in Ref. [18]. More details are given in the Supplemental Material.

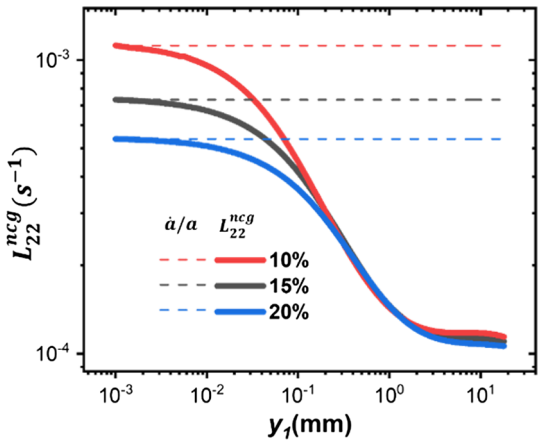

FIG. 11. The $\boldsymbol{L}_{22}^{\mathrm{ncg}}$ (to be identified with $D_{xx,\mathrm{FEM}}$ in the main text) and $\dot{a}/a$ at different ε_N plotted in a double logarithmic scale.

APPENDIX B: SIMULATED STRAIN-RATE FIELD CLOSE TO THE CRACK TIP

Note that $\boldsymbol{L}_{22}^{\mathrm{ncg}}$ (ncg = no crack growth) at different ε_N are plotted in Fig. 11, corresponding to $D_{\mathrm{xx,FEM}}$ in the main text. The dashed lines are the asymptotic result ($\dot{a}/a$ and $y_1\to 0$) predicted by theory and determined numerically, as shown in Eq. (52) and Fig. S11(c), respectively, in Supplemental Material. They are consistent with the FEM result obtained by computing the velocity gradient tensor directly. We also discovered the following (i) Far away from the tip ($y>0.1$ mm), $\boldsymbol{L}_{22}^{\mathrm{ncg}}$ is almost independent of ε_N; (ii) close to the tip ($y<0.1$ mm), a slight decrease of $\boldsymbol{L}_{22}^{\mathrm{ncg}}$ with increasing ε_N can be observed.

APPENDIX C: DYNAMICS ANALYSIS OF DELAYED FRACTURE UNDER STATIC CONDITIONS

Under static conditions, the bulk relaxation plays an important role in the dynamics measured by MSDWS since the majority of the sample remains static during the measurement, free of the influence of the crack. The dynamics localized around the crack tip is influenced by both the bulk relaxation of the sample and the changes in elastic field due to the molecular damage. In this case, the DAM only provides a qualitative visualization of the degree of localization of the dynamics, rather than a quantitative mapping of the strain rate. To separate the effect of bulk relaxation and better visualize the damage or dynamics localization, we first fit the characteristic relaxation time τ_0 in Eq. (A2) in regions far away from the crack tip and use τ_0 as a reference to choose τ_{MSDWS}. In this way, we estimate as precisely as possible the area having dynamics faster than in the bulk, assuming that this faster activation is due to the presence of local damage.

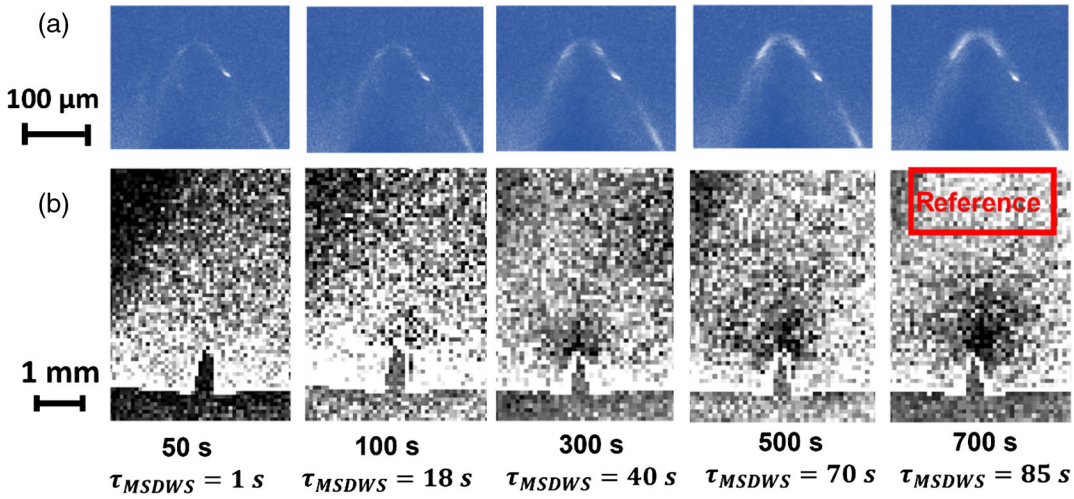

FIG. 12. Imaging of a poly (ethyl acrylate) sample after stretched to $\varepsilon_N = 15\%$. (a) Mechanophore maps around the tip, measured by confocal microscopy and averaged over 50 s. (b) DAM during the crack propagation, with τ_{MSDWS} fitted from the reference rectangular region. Each DAM is labeled by the corresponding t_w value.

1. Case of poly (ethyl acrylate) elastomer

Poly (ethyl acrylate) (PEA) was synthesized through UV-initiated free radical polymerization following a previously reported procedure [27]. Ethyl acrylate monomer was mixed with TiO_2 nanoparticles (1 wt%), cross-linker 1,4-butanediol diacrylate (BDA, 0.5 mol%), UV initiator 2-Hydroxy-2-methylpropiophenone (1.16 mol%), and Diels-Alder adduct mechanophore diacrylate cross-linker (DACL) (0.02 mol%) [12]. The mixture was injected into a mold with thickness of 1 mm and polymerized under UV (10 $\mu W/cm^2$) for 2 h. The Young's modulus was $E = 0.47$ MPa, measured by uniaxial extension (without the notch). Because of the sedimentation of nanoparticles in the mixture with low viscosity, the final nanoparticle concentration in the bulk was less than 1 wt% and hard to quantify. The elastomer was then dried under vacuum overnight before usage, cut into rectangles, and prenotched for single edge notch fracture tests: length of 10 mm between clamps, width of 6 mm, and initial crack length of 1 mm. The frame rate was 5 s/scan.

We studied only the fracture behavior in static measurements since it provides an ideal condition for damage visualization in this soft material, exhibiting little molecular damage in the bulk. The sample was loaded to $\varepsilon_N = 15\%$ and held for a long time for observation, with the setup shown in Fig. 1(a). Figure 12(a) shows the activation intensity measured by confocal microscopy. A slight propagation was observed after 700 s, with an increasing fluorescence intensity around the crack tip.

The relaxation time $\tau_0(t_w)$, obtained by fitting data from the reference region indicated in Fig. 12(b), is shown in Fig. 13. The relaxation time increased almost linearly with t_w, corresponding to the continuous slowing down of the bulk dynamics. DAMs with $\tau_{\mathrm{MSDWS}} \approx 0.2\ \tau_0$ were converted to grayscale as shown in Fig. 12(b), where the lower intensity in DAMs corresponds to faster dynamics. Fast dynamics (lower intensity) in DAMs can be detected over an initial surface around 1 mm^2 ($t_w = 300$ s), increasing to around 6 mm^2 at $t_w = 700$ s.

Even though the crack starts propagating right after the sample is deformed, the propagation is extremely slow, with less than 30 microns of increasing crack length over 1000 s. The increment of the crack length is calculated from mechanophore images and plotted in Fig. 14. An acceleration of the rate of propagation of the crack can be observed after around $t_w = 1200$ s, where the propagation rate jumps from 40 nm/s to 300 nm/s. The sudden acceleration of crack propagation should be related to the accumulation of molecular damage from 0 to 1200 s, as seen in Fig. 12(a). The effect of a slight propagation during the first 1000 s can be decoupled from the accumulation of molecular damage, as pointed out in the FEM simulation.

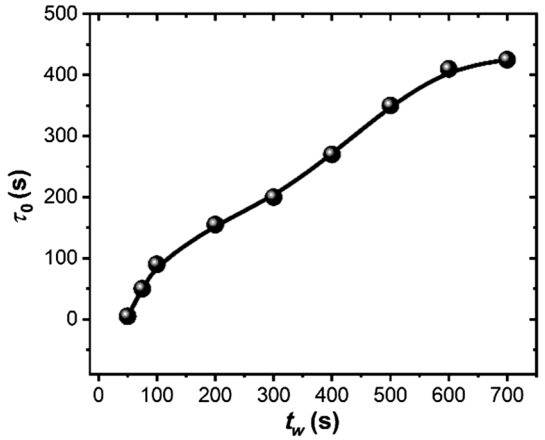

FIG. 13. Relaxation time τ_0 obtained by fitting Eq. (A2) to the MSDWS data in the reference bulk region indicated in Fig. 12 as a function of t_w.

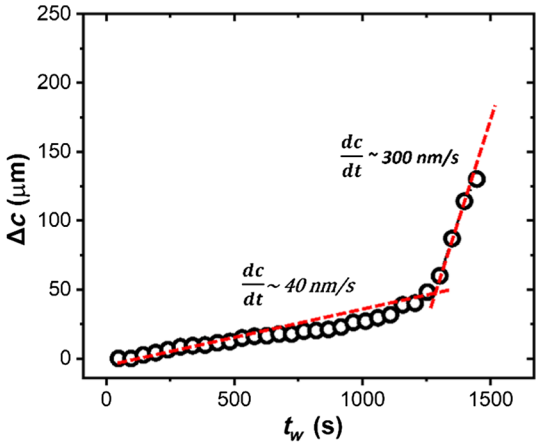

FIG. 14. Propagation length Δc as a function of t_w.

2. PDMS case

The evolution of $\tau_0(t_w)$ in the bulk region of PDMS during the holding time at $\varepsilon = 15\%$ (Fig. 6) is shown in Fig. 15, which shows that, in the bulk, τ_0 exceeds several hundreds of seconds after $t_w = 1000$ s. Thus, the bulk dynamics are much slower compared to those related to a possible crack localization, and we can safely use $\tau_{\mathrm{MSDWS}} = 40$ s for all the DAM of Fig. 6(a). Although bulk dynamics slows with waiting time, the localized area around the crack with significantly faster dynamics than the bulk increases monotonically, and the quantification in Fig. 6(b) is reliable.

The change of crack length Δc is plotted in Fig. 16. The crack starts to slowly propagate (20 nm/s) at around 0.5 hh and slows down (to 3 nm/s) at around 1.5 h. In this example, there is no macroscopic propagation leading to a macroscopic failure of the sample over the whole duration of the step ($t_w = 5$ h), although a longer observation time would probably lead to failure.

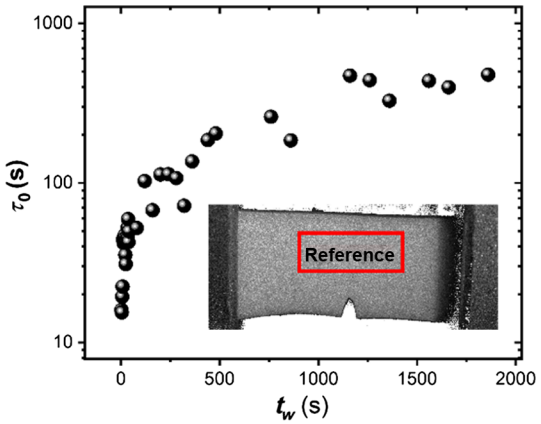

FIG. 15. Relaxation time τ_0 in the bulk region of PDMS in Fig. 6 as a function of t_w.

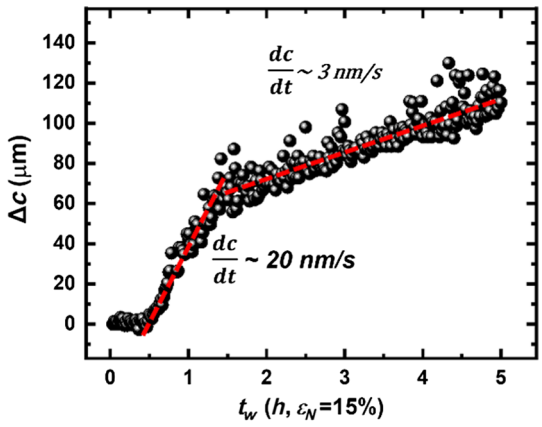

FIG. 16. Propagation length Δc as a function of t_w for the PDMS experiment of Fig. 6.

3. Subsummary

Interestingly, when comparing the respective behaviors of PEA and PDMS, we find that a slower response in the fracture precursor of PDMS corresponds to a slowing down of the propagation (Fig. 16) at long timescales, while an earlier dynamics localization in PEA and its rapid growth correspond to an acceleration of the propagation (Fig. 14). Even though we discuss here two totally different materials, this points out the possibility that the long-term behavior in delayed fracture can be predicted by the accumulation mode of the damage at a very early stage. A reliable model for this discussion needs more data and theoretical analysis, which is beyond the scope of this work.

APPENDIX D: FRACTURE PRECURSOR IN PDMS WITH DIFFERENT MODULI

Fracture precursors before crack propagation were measured in PDMS (Sylgard 184) prepared with different curing agent concentrations (Φ), varying from 0.0625 (15:1 of base-curing agent ratio) to 0.25 (3:1) [Φ is 0.091 (10:1) in the main text], using $\dot{\varepsilon}_N = 10^{-4}$ s^{-1}.

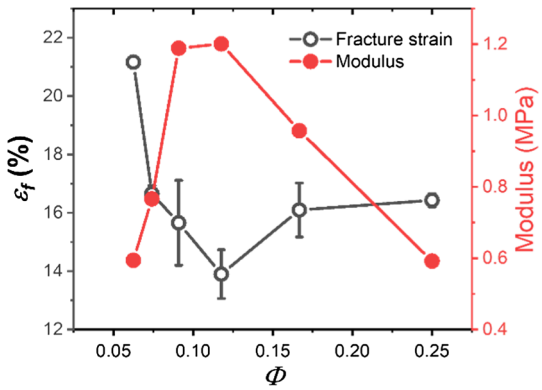

FIG. 17. Fracture strain ε_f and modulus as a function of curing agent concentrations Φ.

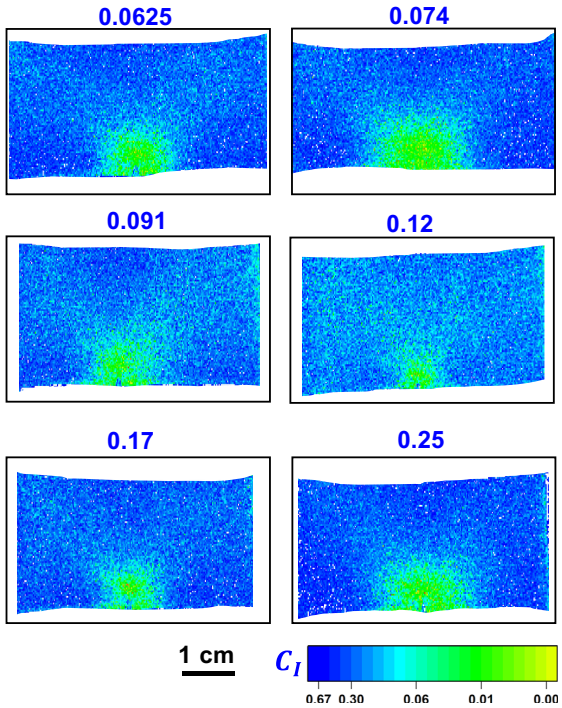

FIG. 18. DAM of single edge notched PDMS samples prepared with $0.0625 < \Phi < 0.25$ (as indicated above each panel), with moduli as shown in Fig. 17. The DAM is taken 20 s before fracture occurs, using $\tau_{\mathrm{MSDWS}} = 0.24$ s.

All samples were cured at 90 °C for 8 h. The critical strain for fracture ε_f and modulus at different Φ are plotted in Fig. 17. It can be found that the modulus peaks at $\Phi \sim 0.12$, where ε_f is the lowest. The nonmonotonic behavior of the modulus as a function of Φ has been reported previously [59,60]. Here, by adjusting Φ, the modulus can be tuned from around 0.6 MPa to 1.2 MPa without significantly changing the damping properties of the elastomer (the viscous component of the complex modulus).

DAMs at 20 s before fracture are shown in Fig. 18, with $\tau_{\mathrm{MSDWS}} = 0.24$ s. The sample size is 2 cm × 4 cm, with an initial crack length of 2 mm. Fracture precursors with comparable sizes can be observed, while the modulus and the fracture strain ε_f both change by about a factor of 2. Note that the size of the high strain-rate region tends to increase with decreasing modulus.

[1] C. Creton and M. Ciccotti, *Fracture and Adhesion of Soft Materials: A Review*, Rep. Prog. Phys. **79**, 046601 (2016).
[2] X. Wang and W. Hong, *Delayed Fracture in Gels*, Soft Matter **8**, 8171 (2012).
[3] S. Mzabi, D. Berghezan, S. Roux, F. Hild, and C. Creton, *A Critical Local Energy Release Rate Criterion for Fatigue Fracture of Elastomers*, J. Polym. Sci. B **49**, 1518 (2011).
[4] R. Bai, J. Yang, and Z. Suo, *Fatigue of Hydrogels*, Eur. J. Mech. Solids **74**, 337 (2019).
[5] L. Vanel, S. Ciliberto, P.-P. Cortet, and S. Santucci, *Time-Dependent Rupture and Slow Crack Growth: Elastic and Viscoplastic Dynamics*, J. Phys. D **42** (2009).
[6] H. M. van der Kooij, S. Dussi, G. T. van de Kerkhof, R. A. Frijns, J. van der Gucht, and J. Sprakel, *Laser Speckle Strain Imaging Reveals the Origin of Delayed Fracture in a Soft Solid*, Sci. Adv. **4**, eaar1926 (2018).
[7] D. Bonn, H. Kellay, M. Prochnow, K. Ben-Djemiaa, and J. Meunier, *Delayed Fracture of an Inhomogeneous Soft Solid*, Science **280**, 265 (1998).
[8] X. Li, K. Cui, T. L. Sun, L. Meng, C. Yu, L. Li, C. Creton, T. Kurokawa, and J. P. Gong, *Mesoscale Bicontinuous Networks in Self-Healing Hydrogels Delay Fatigue Fracture*, Proc. Natl. Acad. Sci. U.S.A. **117**, 7606 (2020).
[9] I. Kolvin, J. M. Kolinski, J. P. Gong, and J. Fineberg, *How Supertough Gels Break*, Phys. Rev. Lett. **121**, 135501 (2018).
[10] Y. Morishita, K. Tsunoda, and K. Urayama, *Velocity Transition in the Crack Growth Dynamics of Filled Elastomers: Contributions of Nonlinear Viscoelasticity*, Phys. Rev. E **93**, 043001 (2016).
[11] Y. Zhang, K. Fukao, T. Matsuda, T. Nakajima, K. Tsunoda, T. Kurokawa, and J. P. Gong, *Unique Crack Propagation of Double Network Hydrogels under High Stretch*, Extreme Mech. Lett. **51**, 101588 (2022).
[12] J. Slootman, V. Waltz, C. J. Yeh, C. Baumann, R. Göstl, J. Comtet, and C. Creton, *Quantifying Rate- and Temperature-Dependent Molecular Damage in Elastomer Fracture*, Phys. Rev. X **10**, 041045 (2020).
[13] A. Duri, D. A. Sessoms, V. Trappe, and L. Cipelletti, *Resolving Long-Range Spatial Correlations in Jammed Colloidal Systems Using Photon Correlation Imaging*, Phys. Rev. Lett. **102**, 085702 (2009).
[14] B. J. Berne and R. Pecora, *Dynamic Light Scattering: With Applications to Chemistry, Biology, and Physics* (Wiley, Hoboken, 1976).
[15] D. Weitz and D. Pine, in *Dynamic Light Scattering: The Method and Some Applications* (Oxford University Press, Oxford, 1993), p. 652.
[16] M. Erpelding, A. Amon, and J. Crassous, *Diffusive Wave Spectroscopy Applied to the Spatially Resolved Deformation of a Solid*, Phys. Rev. E **78**, 046104 (2008).
[17] M.-Y. Nagazi, G. Brambilla, G. Meunier, P. Marguerès, J.-N. Périé, and L. Cipelletti, *Space-Resolved Diffusing Wave Spectroscopy Measurements of the Macroscopic Deformation and the Microscopic Dynamics in Tensile Strain Tests*, Opt. Lasers Eng. **88**, 5 (2017).
[18] J. Ju, L. Cipelletti, S. Zoellner, T. Narita, and C. Creton, *Multispeckle Diffusing Wave Spectroscopy as a Tool to Study Heterogeneous Mechanical Behavior in Soft Solids*, J. Rheol. **66**, 1269 (2022).
[19] A. Duri, H. Bissig, V. Trappe, and L. Cipelletti, *Time-Resolved-Correlation Measurements of Temporally Heterogeneous Dynamics*, Phys. Rev. E **72**, 051401 (2005).
[20] S. Aime, L. Ramos, and L. Cipelletti, *Microscopic Dynamics and Failure Precursors of a Gel under Mechanical Load*, Proc. Natl. Acad. Sci. U.S.A. **115**, 3587 (2018).
[21] A. Pommella, L. Cipelletti, and L. Ramos, *Role of Normal Stress in the Creep Dynamics and Failure of a Biopolymer Gel*, Phys. Rev. Lett. **125**, 268006 (2020).

[22] A. Le Bouil, A. Amon, S. McNamara, and J. Crassous, *Emergence of Cooperativity in Plasticity of Soft Glassy Materials*, Phys. Rev. Lett. **112**, 246001 (2014).

[23] A. Furukawa and H. Tanaka, *Inhomogeneous Flow and Fracture of Glassy Materials*, Nat. Mater. **8**, 601 (2009).

[24] J. Diani, B. Fayolle, and P. Gilormini, *A Review on the Mullins Effect*, Eur. Polym. J. **45**, 601 (2009).

[25] Y. Merckel, J. Diani, M. Brieu, and D. Berghezan, *Experimental Characterization and Modelling of the Cyclic Softening of Carbon-Black Filled Rubbers*, Mater. Sci. Eng. A **528**, 8651 (2011).

[26] E. Ducrot, Y. Chen, M. Bulters, R. P. Sijbesma, and C. Creton, *Toughening Elastomers with Sacrificial Bonds and Watching Them Break*, Science **344**, 186 (2014).

[27] Y. Chen, C. J. Yeh, Y. Qi, R. Long, and C. Creton, *From Force-Responsive Molecules to Quantifying and Mapping Stresses in Soft Materials*, Sci. Adv. **6**, eaaz5093 (2020).

[28] Y. Chen, G. Mellot, D. van Luijk, C. Creton, and R. P. Sijbesma, *Mechanochemical Tools for Polymer Materials*, Chem. Soc. Rev. **50**, 4100 (2021).

[29] X. P. Morelle, G. E. Sanoja, S. Castagnet, and C. Creton, *3D Fluorescent Mapping of Invisible Molecular Damage after Cavitation in Hydrogen Exposed Elastomers*, Soft Matter **17**, 4266 (2021).

[30] G. E. Sanoja, X. P. Morelle, J. Comtet, C. J. Yeh, M. Ciccotti, and C. Creton, *Why is Mechanical Fatigue Different from Toughness in Elastomers? The Role of Damage by Polymer Chain Scission*, Sci. Adv. **7**, eabg9410 (2021).

[31] J. Slootman, C. J. Yeh, P. Millereau, J. Comtet, and C. Creton, *A Molecular Interpretation of the Toughness of Multiple Network Elastomers at High Temperature*, Proc. Natl. Acad. Sci. U.S.A. **119**, e2116127119 (2022).

[32] H. Liebowitz and E. Moyer, Jr., *Finite Element Methods in Fracture Mechanics*, Comput. Struct. **31**, 1 (1989).

[33] V. R. Krishnan, C. Y. Hui, and R. Long, *Finite Strain Crack Tip Fields in Soft Incompressible Elastic Solids*, Langmuir **24**, 14245 (2008).

[34] J. M. Clough, C. Creton, S. L. Craig, and R. P. Sijbesma, *Covalent Bond Scission in the Mullins Effect of a Filled Elastomer: Real-Time Visualization with Mechanoluminescence*, Adv. Funct. Mater. **26**, 9063 (2016).

[35] See Supplemental Material at http://link.aps.org/supplemental/10.1103/PhysRevX.13.021030 for details.

[36] R. Göstl and R. Sijbesma, *π-Extended Anthracenes as Sensitive Probes for Mechanical Stress*, Chem. Sci. **7**, 370 (2016).

[37] G. T. Mase, R. E. Smelser, and G. E. Mase, *Continuum Mechanics for Engineers* (CRC Press, Boca Raton, 2009).

[38] G. C. Johnson and D. J. Bammann, *A Discussion of Stress Rates in Finite Deformation Problems*, Int. J. Solids Struct. **20**, 725 (1984).

[39] T. J. Hughes and J. Marsden, *Mathematical Foundations of Elasticity* (Courier Corporation, North Chelmsford, 1994).

[40] D. André, *pydic*, https://gitlab.com/damien.andre/pydic (2018).

[41] S. R. Lavoie, R. Long, and T. Tang, *A Rate-Dependent Damage Model for Elastomers at Large Strain*, Extreme Mech. Lett. **8**, 114 (2016).

[42] R. Long, V. R. Krishnan, and C.-Y. Hui, *Finite Strain Analysis of Crack Tip Fields in Incompressible Hyperelastic Solids Loaded in Plane Stress*, J. Mech. Phys. Solids **59**, 672 (2011).

[43] G. Lake and A. Thomas, *The Strength of Highly Elastic Materials*, Proc. Math. Phys. Eng. Sci. **300**, 108 (1967).

[44] J. D. Valentin, X.-H. Qin, C. Fessele, H. Straub, H. C. van der Mei, M. T. Buhmann, K. Maniura-Weber, and Q. Ren, *Substrate Viscosity Plays an Important Role in Bacterial Adhesion under Fluid Flow*, J. Colloid Interface Sci. **552**, 247 (2019).

[45] C. Lee, W. A. Take, and N. A. Hoult, *Optimum Accuracy of Two-Dimensional Strain Measurements Using Digital Image Correlation*, J. Comput. Civ. Eng. **26**, 795 (2012).

[46] A. Acciaioli, G. Lionello, and M. Baleani, *Experimentally Achievable Accuracy Using a Digital Image Correlation Technique in Measuring Small-Magnitude (<0.1%) Homogeneous Strain Fields*, Materials **11**, 751 (2018).

[47] M. Sutton, J. Turner, H. Bruck, and T. Chae, *Full-Field Representation of Discretely Sampled Surface Deformation for Displacement and Strain Analysis*, Exp. Mech. **31**, 168 (1991).

[48] B. Winiarski, G. Schajer, and P. Withers, *Surface Decoration for Improving the Accuracy of Displacement Measurements by Digital Image Correlation in SEM*, Exp. Mech. **52**, 793 (2012).

[49] M. Liu, J. Guo, C. Y. Hui, and A. T. Zehnder, *Application of Digital Image Correlation (DIC) to the Measurement of Strain Concentration of a PVA Dual-Crosslink Hydrogel under Large Deformation*, Exp. Mech. **59**, 1021 (2019).

[50] R. Sedlacek and F. A. Halden, *Method for Tensile Testing of Brittle Materials*, Rev. Sci. Instrum. **33**, 298 (1962).

[51] S. L. Phoenix and R. G. Sexsmith, *Clamp Effects in Fiber Testing*, J. Compos. Mater. **6**, 322 (1972).

[52] M. Y. Nagazi, P. Dieudonné-George, G. Brambilla, G. Meunier, and L. Cipelletti, *Phase Transitions in Polymorphic Materials Probed Using Space-Resolved Diffusing Wave Spectroscopy*, Soft Matter **14**, 6439 (2018).

[53] S. Lee and M. Pharr, *Sideways and Stable Crack Propagation in a Silicone Elastomer*, Proc. Natl. Acad. Sci. U.S.A. **116**, 9251 (2019).

[54] C. Marano, M. Boggio, E. Cazzoni, and M. Rink, *Fracture Phenomenology and Toughness of Filled Natural Rubber Compounds via the Pure Shear Test Specimen*, Rubber Chem. Technol. **87**, 501 (2014).

[55] V. Bapst *et al.*, *Unveiling the Predictive Power of Static Structure in Glassy Systems*, Nat. Phys. **16**, 448 (2020).

[56] *ASCII and images of all the data sets shown in the figures in the main text and the Supplemental Material have been deposited in Zenodo*, 10.5281/zenodo.6406808.

[57] D. J. Pine, D. A. Weitz, P. M. Chaikin, and E. Herbolzheimer, *Diffusing Wave Spectroscopy*, Phys. Rev. Lett. **60**, 1134 (1988).

[58] F. Cardinaux, L. Cipelletti, F. Scheffold, and P. Schurtenberger, *Microrheology of Giant-Micelle Solutions*, Europhys. Lett. **57**, 738 (2002).

[59] H. Hocheng, C.-M. Chen, Y.-C. Chou, and C.-H. Lin, *Study of Novel Electrical Routing and Integrated Packaging on Bio-Compatible Flexible Substrates*, Microsyst. Technol. **16**, 423 (2010).

[60] M. L. Fitzgerald, S. Tsai, L. M. Bellan, R. Sappington, Y. Xu, and D. Li, *The Relationship between the Young's Modulus and Dry Etching Rate of Polydimethylsiloxane (PDMS)*, Biomed. Microdevices **21**, 1 (2019).